Journal of Solid State Chemistry 329 (2024) 124376

Contents lists available at ScienceDirect

Journal of Solid State Chemistry

journal homepage: www.elsevier.com/locate/jssc

Two new multinary chalcogenides with $(Se_2)^{2-}$ dimers: $Ba_8Hf_2Se_{11}(Se_2)$ and $Ba_9Hf_3Se_{14}(Se_2)$

Subhendu Jana, Eric A. Gabilondo, Paul A. Maggard *

Department of Chemistry, North Carolina State University, Raleigh, NC, 27695-8204, USA

ARTICLE INFO

Keywords:
Crystal structure
Metal chalcogenide
Optical bandgap
Electronic structure calculations

ABSTRACT

Two multinary selenides, $Ba_8Hf_2Se_{11}(Se_2)$ and $Ba_9Hf_3Se_{14}(Se_2)$, with unprecedented structure types have been prepared using high-temperature synthesis techniques and represent the first known compounds in the Ba-Hf-Se system. Their structures were determined from single crystal X-ray diffraction (XRD) data. The $Ba_8Hf_2Se_{11}(Se_2)$ compound crystallizes in the monoclinic $C2/c$ space group with a = 12.3962(15) Å, b = 12.8928(15) Å, c = 18.1768(17) Å, and β = 90.685(4)°, while $Ba_9Hf_3Se_{14}(Se_2)$ forms in the rhombohedral $R\bar{3}$ space group with $a = b$ = 19.4907(6) Å and c = 23.6407(11) Å. Both have pseudo-zero-dimensional structures with homoatomic Se–Se bonding in the form of $(Se_2)^{2-}$ at distances of 2.400–2.402 Å. The structure of $Ba_8Hf_2Se_{11}(Se_2)$ is comprised of $[Hf_2Se_{11}]^{14-}$, Ba^{2+}, and $(Se_2)^{2-}$ dimers. Conversely, the $Ba_9Hf_3Se_{14}(Se_2)$ structure contains a novel perovskite-type cluster constructed from eight octahedrally-coordinated Hf cations, i.e., $[Hf_8Se_{36}]^{40-}$, and isolated $[HfSe_6]^{8-}$ units which are separated by $(Se_2)^{2-}$ dimers and Ba^{2+} cations. Polycrystalline $Ba_8Hf_2Se_{11}(Se_2)$ is synthesized at 1073 K using a two-step solid-state synthesis method, with the co-formation of a small amount of a BaSe secondary phase. A direct bandgap of 2.2(2) eV is obtained for the polycrystalline sample of $Ba_8Hf_2Se_{11}(Se_2)$, which is consistent with its yellow color. Density functional theory calculations reveal their bandgap transitions stem from predominantly filled Se-4p to empty Hf-5d at the edges of the valence bands (VB) and conduction bands (CB), respectively. The optical absorption coefficients are calculated to be relatively large, exceeding ~10^5 cm^{-1} at about >2.0 eV with effective masses in the CB varying from ~0.5 m_e ($\Gamma \rightarrow A$) in $Ba_8Hf_2Se_{11}(Se_2)$ to ~1.0 m_e ($\Gamma \rightarrow L$) in $Ba_9Hf_3Se_{14}(Se_2)$. Thus, their optoelectronic properties are shown to be competitive with existing perovskite-type chalcogenides that have been a focus of recent research efforts.

1. Introduction

Exploratory synthesis plays a vital role in the solid-state sciences and serves as a powerful tool in unveiling unprecedented structure types and compositions that cannot be predicted in advance. The structural chemistry of chalcogenides (Q = S, Se, and Te) is markedly different from that of oxides, such as showing intriguing catenation properties caused by the larger size and smaller electronegativity of chalcogens [1]. The catenation property of Q atoms leads to the formation of a variety of Q–Q bonding units, such as the occurrence of Q_2^{2-} anions in $Ba_2Ag_2Se_2(Se_2)$ [2], Q_c^{d-} (e.g., Se_5^{4-}, Se_3^{4-}, and Te_5^{4-} polyanions in Nb_2Se_9 [3], $Ba_2Ag_4Se_5$ [4], and Ba_2SnTe_5 [5], respectively), Q_c^{2-} chains (e.g., Te_{12}^{2-} and Te_{13}^{2-} units in $(NEt_4)_2Te_{12}$ [6] and Cs_2Te_{13} [7], respectively), and square-net polyanions in $EuCu_{0.66}Te_2$ [8]). These and many other examples demonstrate how metal chalcogenides can stabilize a variety of polyanion Q motifs leading to a variety of new structure types with interesting physical properties. Synthetic exploration of metal chalcogenides can also play a key role in the establishment of advanced structure-property relationships. The range of observed physical properties has been broad, including nonlinear optical properties, thermoelectric properties, photocatalytic reactivity, magnetic properties, magnetoresistance effects, as well as superconductivity [9–17]. Thus, many metal chalcogenide systems are well established as representing diverse and rich fields for technologically-relevant synthetic explorations.

Recently, the growing interest in the Hf–containing perovskite chalcogenides has been mainly attributed to their complex structures and physical properties, such as thermoelectric properties (e.g., $SrHfSe_3$ [18]), as light-emitting semiconductors (e.g., $SrHfS_3$ [19]), and in semiconductor optoelectronics (e.g., $BaHfS_3$ [20]). Notably, the Hf-containing chalcogenides with perovskite-type structures and compositions have recently been attracting much attention for their

* Corresponding author.
E-mail address: Paul_Maggard@ncsu.edu (P.A. Maggard).

https://doi.org/10.1016/j.jssc.2023.124376
Received 9 August 2023; Received in revised form 2 October 2023; Accepted 4 October 2023
Available online 5 October 2023

promisingly small bandgaps (1.5–2.0 eV) and especially strong band edge absorption, i.e., optical absorption coefficient, $\alpha > 10^5$ cm^{-1}. The limited known examples have included $BaHfS_3$ (*Pnma*) [21], $SrHfS_3$ (*Pnma*) [19,21], and $SrHfSe_3$ (*Pnma*) [18] that form in distorted (non-cubic) perovskite-type structures. By comparison, the oxide compositions $BaHfO_3$ and $SrHfO_3$ crystallize in cubic perovskite-type structures [22,23]. A general literature survey of Hf-containing chemical systems reveals the existence of relatively few compounds in the *Alk*-(Ba or Sr)–Hf–*Q* (*Q* = S, Se, and Te) system, with nearly all occurring in the metal-sulfide systems including $Ba_6Hf_5S_{16}$ [24], $Ba_5Hf_4S_{13}$ [24], Ba_2HfS_4 [25], $Ba_4Hf_3S_{10}$ [26], and $BaHfS_3$ [21]. Surprisingly, no compounds are currently reported to occur in the Ba–Hf–Se ternary system. The hypothetical $BaHfSe_3$ composition with a perovskite-type structure is not yet reported and is predicted to be thermodynamically unstable [27].

As described herein, the recent reports of Hf-containing chalcogenide perovskites have motivated our synthetic exploration of the Ba-Hf-Se and Ba-Hf-O-Se chemical systems for perovskite-type structures and compositions with interesting optical properties. These synthetic investigations have produced two new solid-state compounds, $Ba_8Hf_2Se_{11}(Se_2)$ and $Ba_9Hf_3Se_{14}(Se_2)$, and which represent the first reported compounds in the Ba–Hf–Se system. Both crystallize in new structure types and exhibit $(Se_2)^{2-}$ dimers. Interestingly, $Ba_9Hf_3Se_{14}(Se_2)$ also contains the first known perovskite-type cluster unit, i.e., $[Hf_8Se_{36}]^{40-}$, in analogy to the bulk perovskite-type structure, i.e., $BaHfSe_3$, that is both thermodynamically unstable and has yet to be synthesized. Their electronic structures and optical properties were also probed using density functional theory calculations.

2. Experimental

2.1. Materials used and synthetic procedures

Synthetic reactions were performed using the following starting materials: Ba rod (99+% purity, Alfa Aesar), Hf powder (99.99 % purity, Alfa Aesar), HfO_2 powder (99.5 % purity, Alfa Aesar), and Se powder (99.99 % purity, Alfa Aesar). As some of the starting materials, including Ba and Hf, are air sensitive, the chemical manipulations were conducted inside an Argon-filled dry glove box.

2.1.1. Syntheses of $Ba_8Hf_2Se_{11}(Se_2)$ and $Ba_9Hf_3Se_{14}(Se_2)$ single crystals

Yellow- and red-colored single crystals of $Ba_8Hf_2Se_{11}(Se_2)$ and $Ba_9Hf_3Se_{14}(Se_2)$, respectively, were discovered during an exploratory synthesis in the Ba–Hf–O–Se phase diagram using high-temperature solid-state reactions. One of the reactions containing Ba (257.8 mg, 1.877 mmol), Hf (167.5 mg, 0.938 mmol), HfO_2 (28.2 mg, 0.134 mmol), and Se (296.4 mg, 3.754 mmol) produced the single crystals of both $Ba_8Hf_2Se_{11}(Se_2)$ and $Ba_9Hf_3Se_{14}(Se_2)$. The reactants were loaded into a carbon (C)-coated fused silica tube of 6 mm outer diameter (OD) inside an Ar-filled glove box, and which was then sealed using a torch under dynamic vacuum. The sealed vessel was then placed inside a programmable muffle furnace and heated to 673 K in 4 h, where it was then soaked for 6 h, followed by ramping the temperature to 1223 K in 10 h. The ampoule was annealed at 1223 K for 80 h before switching off the furnace. The furnace was then programmed to cool to room temperature radiatively. The tube was opened in the air, revealing an ingot of polycrystalline product, which was crushed and investigated under an optical microscope.

A few block-shaped red-colored and plate-shaped yellow-colored crystals were selected and picked on carbon tape for elemental analysis using energy-dispersive X-ray (EDX) spectroscopy using a JEOL SEM 6010LA spectrophotometer. An accelerating voltage of 20 kV was used for the EDX data collection. The EDX data on yellow crystals showed the presence of Ba, Hf, and Se in an average ratio of ≈8:2:13, corresponding to the formula of $Ba_8Hf_2Se_{11}(Se_2)$ (Supporting Information, Fig. S1(a)). In contrast, the EDX data of red crystals indicated a formula of $Ba_9Hf_3Se_{14}(Se_2)$ (Ba:Hf:Se ≈ 9:3:16) (Fig. S1(b)). The single crystals of $Ba_8Hf_2Se_{11}(Se_2)$ and $Ba_9Hf_3Se_{14}(Se_2)$ were further reproduced from stoichiometric amounts of starting materials, and the same heating profile was used that was used for the exploratory synthesis. The EDX data was recorded on selected crystals, and unit cell determinations were carried out using single-crystal X-ray diffraction data to confirm their respective compositions.

2.1.2. Syntheses of polycrystalline $Ba_8Hf_2Se_{11}(Se_2)$ and $Ba_9Hf_3Se_{14}(Se_2)$

A two-step, high-temperature solid-state synthesis method was used to prepare a pure polycrystalline $Ba_8Hf_2Se_{11}(Se_2)$ sample. First, stoichiometric amounts of Ba (265.6 mg, 1.934 mmol), Hf (86.3 mg, 0.484 mmol), and Se (248.1 mg, 3.142 mmol) were loaded into a fused silica ampule (12 mm OD) inside the Ar-filled dry glove box. The ampoule was sealed under ~10^{-4} Torr pressure using a flame torch and loaded inside a programmable muffle furnace for heat treatment. The furnace temperature was ramped to 823 K in 6 h and soaked for 12 h before increasing the temperature to 1073 K. The furnace was switched off after annealing for 72 h at 1073 K and cooled to room temperature radiatively. The product was opened in air, revealing a dark homogeneous-looking lump. The product was then ground using an agate mortar pestle inside the Ar-filled dry glove box and pelletized in an ambient atmosphere using a hydraulic press. The pellet was placed inside a carbon-coated fused silica tube and flame sealed under ~10^{-4} Torr pressure. The tube was ramped to 873 K in 2 h and heated for 48 h at 873 K before switching off the furnace, allowing radiative cooling to room temperature. The product was homogeneously ground inside the glove box, and powder X-ray diffraction (PXRD) data were recorded for the polycrystalline sample. The PXRD data confirms the formation of the polycrystalline $Ba_8Hf_2Se_{11}(Se_2)$ phase with a minute secondary phase of BaSe (Fig. 1).

Attempts to synthesize $Ba_9Hf_3Se_{14}(Se_2)$ using stoichiometric amounts of starting materials with the same heating profile used to synthesize $Ba_8Hf_2Se_{11}(Se_2)$ invariably yielded only small quantities of small crystals. The majority phase produced was $Ba_8Hf_2Se_{11}(Se_2)$ along with secondary phases of BaSe. Additional reactions with varying heating profiles produced only impure polycrystalline samples of $Ba_9Hf_3Se_{14}(Se_2)$.

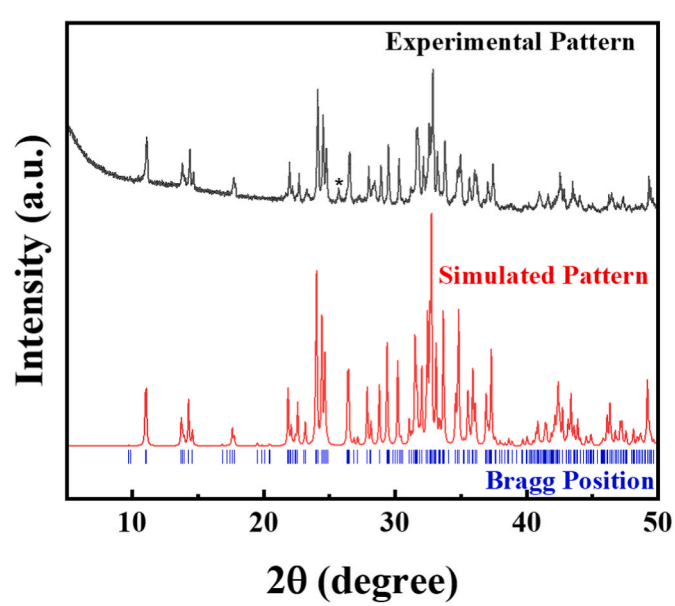

Fig. 1. The simulated (red) and experimental (black) powder X-ray diffraction patterns and Bragg positions for polycrystalline $Ba_8Hf_2Se_{11}(Se_2)$. The (*) peak shows the formation of a minute secondary phase of BaSe.

2.2. X-ray diffraction: Single crystal and polycrystalline powder analyses

The crystal structures of $Ba_8Hf_2Se_{11}(Se_2)$ and $Ba_9Hf_3Se_{14}(Se_2)$ crystals were established by room temperature (300(2) K) single-crystal X-ray diffraction data sets of respective single crystals using a Bruker D8 Venture diffractometer. The intensity data were recorded using a Photon III mixed mode detector and a graphite monochromatized radiation source of Mo-$K\alpha$ ($\lambda = 0.71073$ Å). For each dataset, the $Ba_8Hf_2Se_{11}(Se_2)$ and $Ba_9Hf_3Se_{14}(Se_2)$ crystals were picked separately on a transparent loop under Paratone-N oil and mounted on a goniometer head for data collection. An initial fast scan data of 180 frames were collected to check the crystal quality. The APEX3 software [28] was used to determine the unit cell and collect the data. The intensity data were recorded using a working voltage and working current of 50 kV and 1.4 mA, respectively. An exposure time, frame width, and detector to crystal distance of 2 s/frame, 0.5°, and 50 mm, respectively, were employed during the intensity data collection. APEX3 software was used for the refinement of lattice parameters and integration of the data.

The XPREP software package [29] suggested a *C*-centered monoclinic cell for the $Ba_8Hf_2Se_{11}(Se_2)$ crystal structure. Two space groups were possible based on the extinction conditions: *C2/c* (centrosymmetric) and *Cc* (non-centrosymmetric). The mean statistics of intensity ($|E^2-1|$) value of 0.988 suggested a centrosymmetric space group for the $Ba_8Hf_2Se_{11}(Se_2)$ crystal structure. The expected $|E^2-1|$ values are 0.968 and 0.736 for centrosymmetric and non-centrosymmetric space groups, separately. So, the *C2/c* space group was selected to solve the crystal structure of $Ba_8Hf_2Se_{11}(Se_2)$ using the SHELX-14 [30]. The initial solution of the $Ba_8Hf_2Se_{11}(Se_2)$ crystal structure was obtained using the direct method of the SHELXS program [31]. There were thirteen crystallographically independent atomic positions in the asymmetric unit of the structure, which were further allocated to respective elements based on peak heights, coordination environments, and bond distances. The atomic positions, scale factors, anisotropic displacement parameters, extinction corrections, and weight corrections were further refined using full-matrix least squares on the F^2 method. The final model of the $Ba_8Hf_2Se_{11}(Se_2)$ crystal structure consists of five Ba, one Hf, and seven Se crystallographic sites.

No missing symmetry was found by the ADDSYM program of the PLATON software [32]. The atomic positions were standardized with the help of the STRUCTURE TIDY program [33]. The difference Fourier map of the final solved structure of $Ba_8Hf_2Se_{11}(Se_2)$ is nearly featureless. A small maximum peak of 1.70 $Å^{-3}$ (position: 0.5, 0, 0.5) and the deepest hole of −1.99 $Å^{-3}$ (0.4966, 0.0190, 0.5781) were present at 2.32 Å and 1.68 Å away from the Se(5) atom, respectively. The crystal structure refinement and metric details for the $Ba_8Hf_2Se_{11}(Se_2)$ crystal structure are listed in Tables 1, 2 and 4 and in the Supporting Information.

For the single crystal structure of $Ba_9Hf_3Se_{14}(Se_2)$, the lattice dimensions and extinction conditions were found to be consistent with a rhombohedral (*R*) centrosymmetric cell ($|E^2-1| = 1.083$). So, the $R\,\bar{3}$ space group was selected from the suggested $R\,\bar{3}$ (centrosymmetric) and *R*3 (noncentrosymmetric) space groups. The $Ba_9Hf_3Se_{14}(Se_2)$ crystal structure was solved, refined, and standardized similarly as described earlier for solving the $Ba_8Hf_2Se_{11}(Se_2)$ crystal structure. The asymmetric unit of the crystal structure of $Ba_9Hf_3Se_{14}(Se_2)$ has seventeen crystallographically independent sites: six Ba, three Hf, and eight Se sites. The minimum peak (−2.46 $Å^{-3}$) for the $Ba_9Hf_3Se_{14}(Se_2)$ structure was found at (0.9809, 0.0084, 0.1528), which is 0.49 Å away from the Ba(5) atom. Whereas a small maximum electron density of 1.06$Å^{-3}$ was located 1.17 Å apart from Se(4) (position: 0.1998, 0.6577, 0.0090). The metric and crystal structure refinement details of the $Ba_9Hf_3Se_{14}(Se_2)$ crystal structure are provided in Tables 1, 3 and 4 and in the Supporting Information.

A room temperature powder X-ray diffraction (PXRD) data set was recorded at 300(2) K using a PANalytical Empyrean X-ray diffractometer on a polycrystalline sample of $Ba_8Hf_2Se_{11}(Se_2)$. A Cu-$K\alpha$ radiation source ($\lambda = 1.5406$ Å) was used to collect the data over a 2θ region of 5° to 50°. An operating current and a working voltage of 40 mA and 45 kV were used to record the data with a 0.013° step size.

Table 1
Crystallographic structural data and refinement details for the $Ba_8Hf_2Se_{11}(Se_2)$ and $Ba_9Hf_3Se_{14}(Se_2)$ structures.[a]

	$Ba_8Hf_2Se_{11}(Se_2)$	$Ba_9Hf_3Se_{14}(Se_2)$
Space group	C^6_{2h} −*C2/c*	C^2_{3i} −$R\bar{3}$
a (Å)	12.3962(15)	19.4907(6)
b (Å)	12.8928(15)	
c (Å)	18.1768(17)	23.6407(11)
β (°)	90.685(4)	
V ($Å^3$)	2904.8(6)	7777.6(6)
Z^c	4	9
ρ (g cm^{-3})	5.676	5.832
μ (mm^{-1})	34.04	35.87
$R(F)^b$	0.017	0.022
$R_w(F_o^2)^c$	0.035	0.046
S	1.09	1.06
No. of measured reflections	46188	85356
No. of independent reflections	4424	4283
Reflections with I > 2σ(I)	4180	3716

[a] $\lambda = 0.71073$ Å, $T = 300(2)$ K.
[b] $R(F) = \Sigma\,||F_o|-|F_c||/\Sigma|F_o|$ for $F_o^2 > 2\sigma(F_o^2)$.
[c] $R_w(F_o^2) = \{\Sigma\,[w(F_o^2 - F_c^2)^2]/\Sigma wF_o^4\}^{1/2}$. For $F_o^2 < 0$, $w = 1/[\sigma^2(F_o^2) + (rP)^2 + sP]$; where $P = (F_o^2 + 2F_c^2)/3$. Where *r* and *s* are 15.6886 and 0, and 0.0078 and 191.5368 for $Ba_8Hf_2Se_{11}(Se_2)$ and $Ba_9Hf_3Se_{14}(Se_2)$, respectively.

Table 2
Fractional atomic coordinates and isotropic or equivalent isotropic displacement parameters ($Å^2$) for $Ba_8Hf_2Se_{11}(Se_2)$ structure.

Atom	Wyckoff Position	*x*	*y*	*z*	U_{eq}
Ba (1)	8*f*	0.00582 (2)	0.31184 (2)	0.48577 (2)	0.01325 (4)
Ba (2)	8*f*	0.31856 (2)	0.37530 (2)	0.30850 (2)	0.01334 (4)
Ba (3)	8*f*	0.32104 (2)	0.47585 (2)	0.06435 (2)	0.01317 (4)
Ba (4)	4*e*	0	0.18211 (2)	¼	0.01475 (6)
Ba (5)	4*e*	0	0.54971 (2)	¼	0.01422 (6)
Hf(1)	8*f*	0.25581 (2)	0.17583 (2)	0.13462 (2)	0.00998 (4)
Se(1)	8*f*	0.06516 (3)	0.07558 (3)	0.09675 (2)	0.01257 (7)
Se(2)	8*f*	0.13884 (3)	0.35228 (3)	0.16887 (2)	0.01185 (6)
Se(3)	8*f*	0.24423 (3)	0.11038 (3)	0.27104 (2)	0.01269 (7)
Se(4)	8*f*	0.24907 (3)	0.21674 (3)	0.43828 (2)	0.01515 (7)
Se(5)	8*f*	0.36547 (3)	0.01203 (3)	0.08690 (2)	0.01339 (7)
Se(6)	8*f*	0.43855 (3)	0.28002 (3)	0.15545 (2)	0.01245 (7)
Se(7)	4*c*	¼	¼	0	0.01032 (8)

2.3. Spectroscopic characterization

The Raman spectrum of the polycrystalline $Ba_8Hf_2Se_{11}(Se_2)$ sample was recorded at room temperature (298(2) K) using a Horiba XploRA PLUS confocal microscope equipped with a sincerity OE detector over a wavelength range of 50–3500 cm^{-1}. The excitation wavelength of 532 nm was used to collect the data with a resolution of 3 cm^{-1}.

Solid state ultraviolet–visible (UV–vis) spectra were measured on the polycrystalline $Ba_8Hf_2Se_{11}(Se_2)$ sample after grinding inside an Ar-filled

Table 3
Fractional atomic coordinates and isotropic or equivalent isotropic displacement parameters (Å^2) for the $Ba_9Hf_3Se_{14}(Se_2)$ structure.

Atom	Wyckoff Position	*x*	*y*	*z*	U_{eq}
Ba (1)	18*f*	0.04973 (2)	0.21858 (2)	0.38500 (2)	0.01440(8)
Ba (2)	18*f*	0.06038 (2)	0.27174 (2)	0.16607 (2)	0.01495(8)
Ba (3)	18*f*	0.21106 (2)	0.20301 (2)	0.04771 (2)	0.01510(8)
Ba (4)	18*f*	0.22389 (2)	0.16821 (2)	0.26408 (2)	0.01416(8)
Ba (5)	6*c*	0	0	0.15808 (3)	0.01982 (14)
Ba (6)	3*b*	0	0	½	0.01782 (18)
Hf(1)	18*f*	0.27668 (2)	0.41909 (2)	0.10223 (2)	0.01041(6)
Hf(2)	6*c*	0	0	0.31314 (2)	0.01105(9)
Hf(3)	3*a*	0	0	0.000000	0.01173 (12)
Se(1)	18*f*	0.00712 (4)	0.11716 (4)	0.06566 (2)	0.01496 (12)
Se(2)	18*f*	0.03215 (4)	0.12950 (4)	0.25344 (2)	0.01414 (12)
Se(3)	18*f*	0.06543 (4)	0.35880 (4)	0.29711 (3)	0.01687 (13)
Se(4)	18*f*	0.11703 (3)	0.09044 (3)	0.37959 (2)	0.01320 (12)
Se(5)	18*f*	0.15182 (4)	0.33905 (4)	0.03686 (2)	0.01387 (12)
Se(6)	18*f*	0.18910 (3)	0.46024 (4)	0.16703 (2)	0.01263 (12)
Se(7)	18*f*	0.24757 (4)	0.30590 (4)	0.17387 (2)	0.01434 (12)
Se(8)	18*f*	0.27633 (4)	0.12382 (4)	0.13873 (3)	0.01684 (13)

Table 4
Selected nearest-neighbor bond distances for the $Ba_8Hf_2Se_{11}(Se_2)$ and $Ba_9Hf_3Se_{14}(Se_2)$ structures.

$Ba_8Hf_2Se_{11}(Se_2)$		$Ba_9Hf_3Se_{14}(Se_2)$	
Atom pair	Bond distance (Å)	Atom pair	Bond distance (Å)
Hf(1)–Se(3)	2.6249(4)	Hf(1)–Se(7)	2.6088(6)
Hf(1)–Se(7)	2.6273(3)	Hf(1)–Se(3)	2.6236(6)
Hf(1)–Se(6)	2.6569(4)	Hf(1)–Se(5)	2.6359(6)
Hf(1)–Se(5)	2.6624(4)	Hf(1)–Se(6)	2.6555(6)
Hf(1)–Se(2)	2.7725(4)	Hf(1)–Se(4)	2.6603(6)
Hf(1)–Se(1)	2.7732(4)	Hf(1)–Se(6)	2.6969(6)
Se(4)–Se(4)	2.4018(7)	Hf(2)–Se(4)	2.5994(6) × 3
		Hf(2)–Se(2)	2.6784(6)
		Hf(2)–Se(2)	2.6785(6) × 2
		Hf(3)–Se(1)	2.7068(6) × 6
		Se(8)–Se(8)	2.3999(13)

glove box to make a homogenized powder. A Shimadzu 3600 UV–vis–NIR spectrophotometer was used to collect the reflectance data over a wavelength range of 1000 nm (1.24 eV) to 250 nm (4.96 eV). The dried $BaSO_4$ powder was used as the standard reference for the data collection. The Kubelka-Munk equation [34]: $\alpha/S = (1\text{-}R)^2/2R$ was used to convert the reflectance data to absorption data. Here S, α, and R are the scattering coefficient, absorption coefficient, and reflectance, respectively. Tauc plots [35] were used to evaluate the optical bandgap for the polycrystalline $Ba_8Hf_2Se_{11}(Se_2)$ sample:

$$(\alpha h\upsilon)^n = A(h\upsilon - E_g) \quad (1)$$

In equation (1), the terms h, υ, A, and E_g represent Planck's constant, frequency of light, proportionality constant, and bandgap. The value of constant n indicates the nature of the bandgap. The $n = 2$ and ½ values indicate direct and indirect bandgaps, respectively.

2.4. Electronic structure calculations

Density functional theory calculations were performed with the use of the Projector Augmented Wave (PAW) method within the Vienna *Ab Initio* Simulation Package (VASP) software package [36,37]. The generalized gradient approximation (GGA) was used to treat the exchange-correlation functionals [38]. The criteria for energy convergence was set to 10^{-8} eV and the cutoff energy was fixed to 520 eV in accordance with the PAW pseudopotentials for the Ba, Hf, and Se contributions. Full geometry relaxations utilized a Γ-centered 4 × 4 × 4 *k*-point mesh and 36 *k*-points. Individual atomic orbital contributions were projected out in the calculated Densities-of-States (DOS). Calculations of the band structures were performed using 10 intersections along the standard high symmetry directions [39] of the conventional *k*-point path within the Brillouin zone of the respective crystals systems for the primitive cells of $Ba_8Hf_2Se_{11}(Se_2)$ (i.e., Γ-Y-M-A-Γ|L2-Γ-V2) and $Ba_9Hf_3Se_{14}(Se_2)$ (i.e., Γ-L-T|P2-Γ-F). The Crystal Orbital Hamilton Populations (COHP) of the Hf−Se and Se–Se interactions were calculated with the use of the LOBSTER (Local-Orbital Suite Towards Electronic-Structure Reconstruction) software package version 4.1.0 [40–44].

3. Results and discussion

3.1. Syntheses and crystal structures

Two multinary chalcogenides, $Ba_8Hf_2Se_{11}(Se_2)$ and $Ba_9Hf_3Se_{14}(Se_2)$, with new structure types have been obtained during a synthetic exploration of the Ba–Hf–Se system by high-temperature reactions of the elements at 1223 K. These compounds represent the first reported chalcogenides in this chemical system. Stoichiometric reactions yielded $Ba_8Hf_2Se_{11}(Se_2)$ and $Ba_9Hf_3Se_{14}(Se_2)$ as yellow and red crystals, respectively, but in relatively high purity (~80 %) only for the former. Reactions loaded on the $Ba_9Hf_3Se_{14}(Se_2)$ composition mainly produced yellow plates of $Ba_8Hf_2Se_{11}(Se_2)$ along with small amounts of red-colored blocks of $Ba_9Hf_3Se_{14}(Se_2)$ in ~5–10 % yield. The polycrystalline phase of $Ba_8Hf_2Se_{11}(Se_2)$ was synthesized at 1073 K using a two-step sealed tube solid-state synthesis method. Both compounds appear stable in air for a period of days with no detectable decomposition.

The crystal structure of $Ba_8Hf_2Se_{11}(Se_2)$ was characterized by room temperature single crystal X-ray diffraction data. It was found to crystallize in a new structure type in the *C*2/*c* space group with unit cell parameters of $a = 12.3962(15)$ Å, $b = 12.8928(15)$ Å, $c = 18.1768(17)$ Å, and $\beta = 90.685(4)^\circ$ with four formula units in the unit cell ($Z = 4$). There are thirteen crystallographically-independent atomic sites: five Ba, one Hf, and seven Se sites. The list of atomic coordinates and isotropic displacement parameter are given in Table 2. A structural view of the unit cell of $Ba_8Hf_2Se_{11}(Se_2)$ is shown in Fig. 2(a):

The Hf atoms are coordinated within distorted $HfSe_6$ octahedra which are vertex-bridged through Se(7) to form a dimer unit with the anionic motif of $[Hf_2Se_{11}]^{14-}$, illustrated in Fig. 2(b). The Hf−Se distances in the $HfSe_6$ octahedra range from 2.6249(4) Å to 2.7732(4) Å, which compare reasonably well with Hf−Se distances in previously reported compounds such as $SrHfSe_3$ (2.559(2)–2.720(9) Å) [18], $NaCuHfSe_3$ (2.608(1)–2.788(1) Å) [45], and $NaCuHf_2Se_5$ (2.65(1)–2.701(2) Å) [46]. Also, the distance between neighbouring Se(4) atoms of 2.4018(7) Å is indicative of the presence of Se–Se bonding and formation of $(Se_2)^{2-}$ dimers. The Pauling covalent radii [47] of a Se atom is ~1.17 Å, and thus two Se atoms have a total Pauling covalent radius of ~2.34 Å. The Se–Se bond distance can be compared to previously reported examples found in $Ba_2Ag_2Se_2(Se_2)$ (2.378(2) Å) [2], $Ba_3ThSe_3(Se_2)$ ((2.374(1) Å and 2.377(1) Å) [48], and $CsAuSe_3$ (2.384(1) Å)

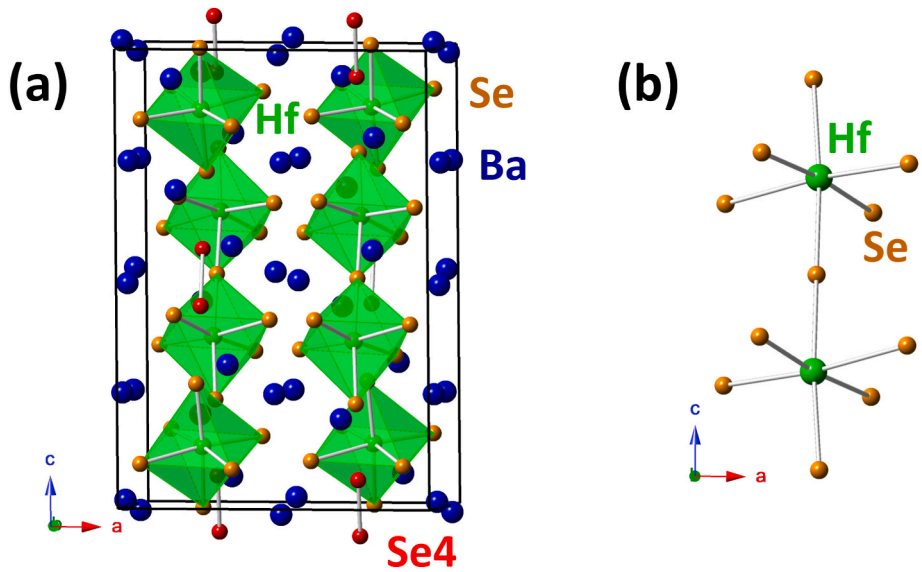

Fig. 2. A structural view of the (a) unit cell of $Ba_8Hf_2Se_{11}(Se_2)$ approximately along the [010] direction and (b) the $[Hf_2Se_{11}]^{14-}$ dimeric units.

[49]. This leads to a charge-balanced formula consisting of Ba^{2+} and Hf^{4+} cations, as well as both Se^{2-} and Se_2^{2-} anions. Details of the respective Ba cation coordination environments are provided in the Supporting Information.

The second known compound in the Ba-Hf-Se system, $Ba_9Hf_3Se_{14}(Se_2)$, was found to crystallize in the rhombohedral $R\bar{3}$ space group with the unit cell parameters $a = b = 19.4907(6)$ Å and $c = 23.6407(11)$ Å with nine formula units ($Z = 9$) in the unit cell. There are seventeen crystallographically-independent atomic positions, including six Ba, three Hf, and eight Se sites. A listing of atomic coordinates and isotropic displacement parameter is given in Table 3, with nearest-neighbor distances given in Table 4.

A structural view of the unit cell of $Ba_9Hf_3Se_{14}(Se_2)$ is illustrated in Fig. 3(a). In the $Ba_9Hf_3Se_{14}(Se_2)$ crystal structure, every Hf atom has six nearest-neighbor Se atoms, forming distorted $HfSe_6$ octahedra. The structure consists of isolated $[HfSe_6]^{8-}$ octahedra as well as perovskite-like $[Hf_8Se_{36}]^{40-}$ cluster anions, shown in Fig. 3(b, c and d) respectively. In the former, the Hf(3)-centered $[HfSe_6]^{8-}$ octahedra exhibit Hf−Se distances of 2.7068(6) Å. Although all Hf(3)–Se(1) interatomic distances are the same, the octahedral units are slightly distorted because of the Se(1)–Hf(3)–Se(1) bond angles (Table S4). In the perovskite-like $[Hf_8Se_{36}]^{40-}$ clusters, the Hf−Se distances range from 2.6088(6) Å to 2.6969(6) Å and 2.5994(6) Å to 2.6785(6) Å for Hf(1)-centered and Hf(2)-centered octahedra, respectively. The vertex-bridged condensation of the $Hf(1)Se_6$ and $Hf(2)Se_6$ octahedra leads to the formation of the $[Hf(1)_6Hf(2)_2Se_{36}]^{40-}$ perovskite cluster, including 12 vertex-bridging and 24 terminal selenide anions. Interestingly, the perovskite-like $[Hf_8Se_{36}]^{40-}$ cluster of the $Ba_9Hf_3Se_{14}(Se_2)$ crystal structure is like that known for the perovskite-type $BaHfS_3$ structure, wherein the Ba^{2+} cations are located within a cuboctahedral environment of eight vertex-bridging HfS_6 octahedra. The analogous selenide, i.e., $BaHfSe_3$ in a perovskite-type structure, is not reported to occur because of an unfavorable tolerance factor and the lack of thermodynamic stability [27]. Most interestingly, the formation of perovskite-like $[Hf_8Se_{36}]^{40-}$ clusters can be stabilized for the first time within this selenium-richer structure. As described above for $Ba_8Hf_2Se_{11}(Se_2)$, Se–Se bond distance of 2.3999(13) Å are also found in its structure and indicating the presence of Se–Se bonding in the form of $(Se_2)^{2-}$ dimers. This distance is similar to that found in prior reported structures, as probed in further detail below using electronic structure calculations.

Charge balancing of both compounds can be achieved by considering Ba, Hf, and Se in their closed-shell electronic configurations and consideration of the homoatomic Se–Se bonding. The short nearest-neighbor Se–Se bonding occurs in both the $Ba_8Hf_2Se_{11}(Se_2)$ (Se(4)–Se(4) = 2.4018(7) Å) and $Ba_9Hf_3Se_{14}(Se_2)$ (Se(8)–Se(8) = 2.3999(13) Å) crystal structures, i.e., forming $(Se_2)^{2-}$ anionic dimers. All other Se

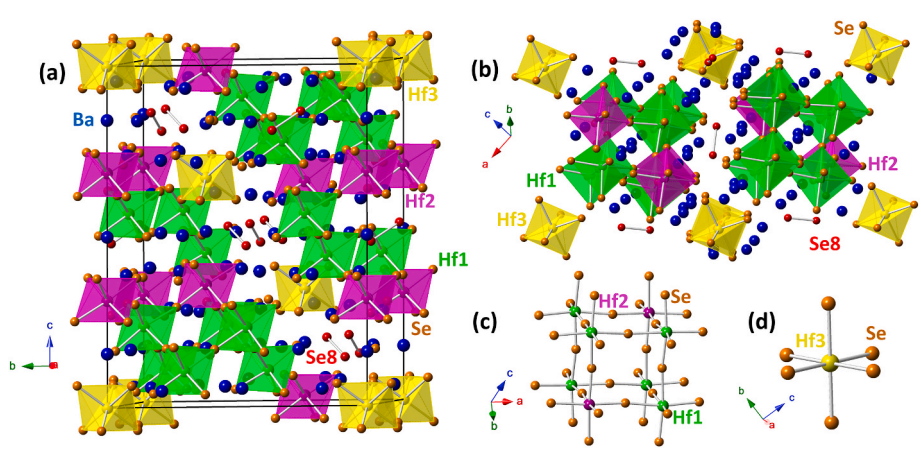

Fig. 3. A structural view of the (a) unit cell of the $Ba_9Hf_3Se_{14}(Se_2)$ structure, (b, c) packing of the individual perovskite-like $[Hf_8Se_{36}]^{40-}$ clusters (purple and green octahedra) and (d) $[HfSe_6]^{8-}$ units (yellow octahedra). All Hf-centered polyhedra are colored green, yellow or purple.

atoms are considered to be in their −2 oxidation state. There is no homoatomic or heteroatomic bonding between the electropositive Ba and Hf atoms, which indicates that the Ba and Hf atoms are present in their +2 and + 4 oxidation states, respectively. So, the charge balancing for the $Ba_8Hf_2Se_{11}(Se_2)$ structure can be considered as $(Ba^{2+})_8(Hf^{4+})_2(Se^{2-})_{11}(Se_2)^{2-}$. Whereas $Ba_9Hf_3Se_{14}(Se_2)$ can be charge balanced as $(Ba^{2+})_9(Hf^{4+})_3(Se^{2-})_{14}(Se_2)^{2-}$. Additional details are provided in the electronic structure calculations, as described below.

3.2. Spectroscopic characterization methods

Measurements of elemental compositions using energy dispersive X-ray spectroscopy on yellow crystals of $Ba_8Hf_2Se_{11}(Se_2)$ yielded only the occurrence of Ba, Hf, and Se in an average ratio of ≈8:2:13, consistent with its chemical formula. Similar measurements on red crystals of $Ba_9Hf_3Se_{14}(Se_2)$ also gave an elemental composition of ≈9:3:16 for Ba:Hf:Se molar ratio, consistent with its chemical formula. The EDS spectrum for each is provided in the Supporting Information. A room-temperature Raman spectrum was acquired for polycrystalline $Ba_8Hf_2Se_{11}(Se_2)$ in the wavelength region of 50–3500 cm^{-1} (Fig. 4). The Raman spectrum showed an intense band at 250 cm^{-1}, which is indicative of the Se–Se stretching mode of Se_2^{2-} unit in $Ba_8Hf_2Se_{11}(Se_2)$. The vibration of the Se_2^{2-} unit of $Ba_8Hf_2Se_{11}(Se_2)$ compares well with the Se–Se stretching mode of K_2Se_2 (~253 cm^{-1}) [50], $Ba_4SiSb_2Se_{11}$ (~247 cm^{-1}) [51], and $Ba_2Ag_2Se_2(Se_2)$ (~247 cm^{-1}) [2]. The bands at ~147 cm^{-1} and 200 cm^{-1} in the Raman spectrum of $Ba_8Hf_2Se_{11}(Se_2)$ stem from the Hf–Se stretching mode in $Ba_8Hf_2Se_{11}(Se_2)$, which agrees well with the Hf–Se stretching modes at ~146 cm^{-1} and 199 cm^{-1} in $HfSe_2$ [52]. The other peaks below 200 cm^{-1} can be assigned to various Ba–Se stretching modes [53]. All Raman stretches are generally consistent with its composition and structure.

The yellow and red-colored crystals of $Ba_8Hf_2Se_{11}(Se_2)$ and $Ba_9Hf_3Se_{14}(Se_2)$, respectively, indicated both compounds are intrinsic semiconductors. To probe the band transitions of $Ba_8Hf_2Se_{11}(Se_2)$, room temperature optical absorption data were collected in diffuse reflectance mode over a wavelength range of 1000 nm (1.24 eV) to 250 nm (5.94 eV). The direct and indirect band transitions were determined using Tauc plots [35] of the absorption data, shown together in Fig. 4(b) for both the direct and indirect transitions. A direct transition energy of ~2.2(2) eV is found for $Ba_8Hf_2Se_{11}(Se_2)$, consistent with its yellow color. A similar Tauc plot of its indirect transition yielded a lower energy ~1.5(2) eV, thus showing the indirect nature of the band gap for $Ba_8Hf_2Se_{11}(Se_2)$. Sufficiently pure samples of $Ba_9Hf_3Se_{14}(Se_2)$ could not be obtained for unambiguous Raman and UV–Vis diffuse reflectance measurements.

3.3. Electronic structure calculations

Research into chalcogenide-based perovskite semiconductors has experienced growing interest owing to their strong band-edge absorption (optical absorption coefficient, $\alpha > 10^5$ cm^{-1}) and small bandgaps of ~1.5–2.0 eV [21,27]. Though, relationships to their crystal structures and impacts upon the nature and strength of their optical bandgap transitions have not been well explored. Density functional theory calculations were employed to probe the electronic structures, band gaps, and the underlying chemical bonding in $Ba_8Hf_2Se_{11}(Se_2)$ and $Ba_9Hf_3Se_{14}(Se_2)$, and usefully serving as a comparison of the non-perovskite-type structures in this Ba-Hf-Se chemical system.

Both structures were first geometry optimized followed by subsequent, separate calculations of their band structures and Density-of-States (DOS) using k-points along a conventional high-symmetry path or randomly distributed, respectively. Shown in Fig. 5 (a and b) are the calculated DOS plots for each structure, with the individual atomic orbital contributions shown for Se (green), Hf (red) and Ba (brown). These show that the edges of the valence bands (VB) consist of filled Se-based states, while the edges of the conduction bands (CB) are comprised of empty Hf-based states. The latter is mixed, at higher energies, with a minor but increasing contribution from Se-based states, further described below. The bandgap of $Ba_8Hf_2Se_{11}(Se_2)$ was calculated to be ~1.61 eV (indirect; Γ-point to F-point), in close agreement with the optical diffuse reflectance data in Fig. 4. The direct transition is found to be less than ~0.1 higher in energy, likely resulting from the underestimation of band transitions that has been well documented [54]. For $Ba_9Hf_3Se_{14}(Se_2)$, the bandgap was calculated to be smaller, ~1.55 eV (direct; Γ-point), and generally consistent with its reddish color. The calculated band structures, Figs. S4 and S5, are given in the Supporting Information. The smallest effective masses in the CB of each were ~0.5 m_e^* (Γ → A) in $Ba_8Hf_2Se_{11}(Se_2)$ and ~1.0 m_e^* (Γ → L) in $Ba_9Hf_3Se_{14}(Se_2)$. This compares similarly to electron effective masses within chalcogenide perovksites that have recently been intensely investigated for optoelectronic applications, such as in $BaHfS_3$ (~0.94 m_e^*) and $BaZrS_3$ (~0.41 m_e^*) [55]. Further, the computed optical absorption coefficients, shown plotted in Fig. 5 (c and d), were found to be surprisingly large. Both exceed ~10^5 cm^{-1} at photon energies greater than 2.0 eV. Similarly, the optical absorption coefficients of analogous chalcogenide perovskites reach optical absorption coefficients of >10^5 cm^{-1} for photon energies greater than 2.0 eV, e.g., such as calculated for $BaZrS_3$ [27,55]. Thus, these results demonstrate absorption coefficients and small effective masses that are competitive with the multinary chalcogenides with perovskite-type structures.

Computations of the Crystal Orbital Hamilton Populations were performed using density functional theory on the geometry relaxed structures of $Ba_8Hf_2Se_{11}(Se_2)$ and $Ba_9Hf_3Se_{14}(Se_2)$ to probe the Hf−Se and Se–Se interactions (i.e., in the $(Se_2)^{2-}$ dimers) within each. The

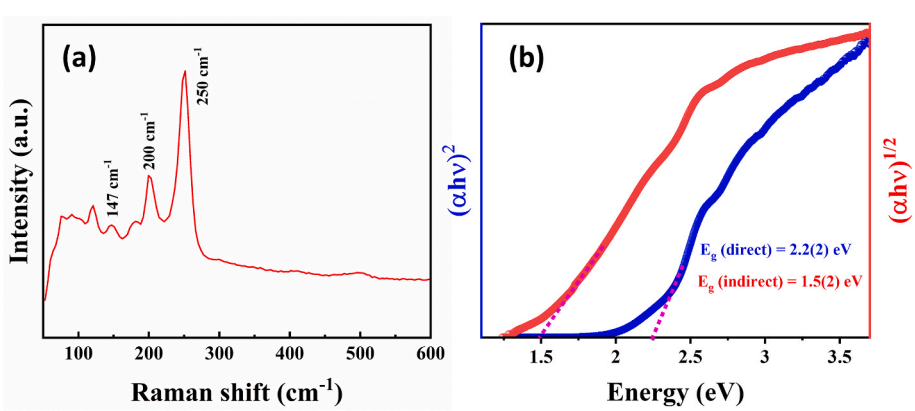

Fig. 4. Raman spectrum (a) and Tauc plots (b) for a polycrystalline sample of $Ba_8Hf_2Se_{11}(Se_2)$.

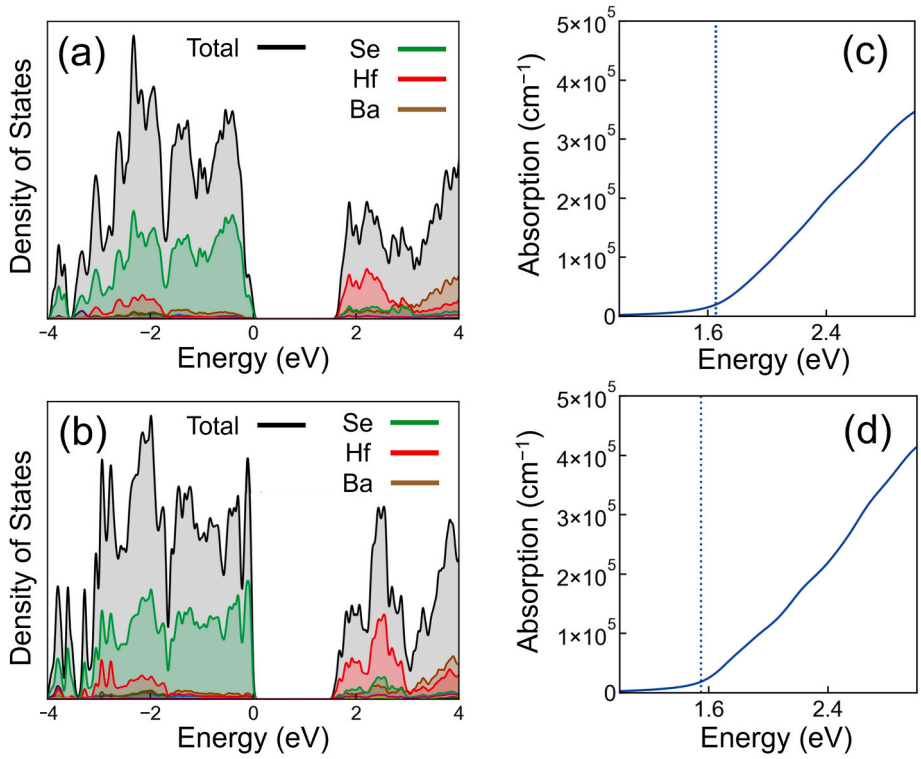

Fig. 5. Calculated electronic density-of-states (DOS) plots for the (a) $Ba_8Hf_2Se_{11}(Se_2)$ and (b) $Ba_9Hf_3Se_{14}(Se_2)$ crystal structures and (c, d) their respective optical absorption coefficients versus energy. For (a) and (b) the Fermi levels are located at 0 eV, while in (c) and (d) the bandgap energy is labelled by the dashed blue line.

results are plotted together in Fig. 6, showing the bonding (+) and antibonding (−) populations as a function of energy with respect to the Fermi level. Both show optimization of the Hf−Se interactions (red colored), with bonding states fully occupied and the antibonding states empty. This confirms the small but growing Se contributions to the conduction bands at increasing energies, Fig. 5 (a and b), is the result of antibonding Hf−Se interactions. Conversely, the Se–Se interactions in the $(Se_2)^{2-}$ dimers, Fig. 6 (blue colored) show an occupation of antibonding states near the top of the valence bands, as well as empty antibonding states at the bottom of the conduction bands. The crystal orbital bond indices (COBI) [56], an analogue for bond order in extended systems, for the Se–Se dimer interactions were calculated to be 0.808 and 0.819 in $Ba_8Hf_2Se_{11}(Se_2)$ and $Ba_9Hf_3Se_{14}(Se_2)$, respectively. These are generally consistent with single bonds, formally, in the $(Se_2)^{2-}$ dimers, as would be expected from electron counting. Further, the contributions of the Se–Se antibonding states, shown to occur at the edges of the conduction and valence bands, may also likely contribute to the large optical absorption coefficients and small bandgaps of both compounds. Future investigations are warranted and underway to probe the impact of the structural units of multinary chalcogenides on their optoelectronic properties.

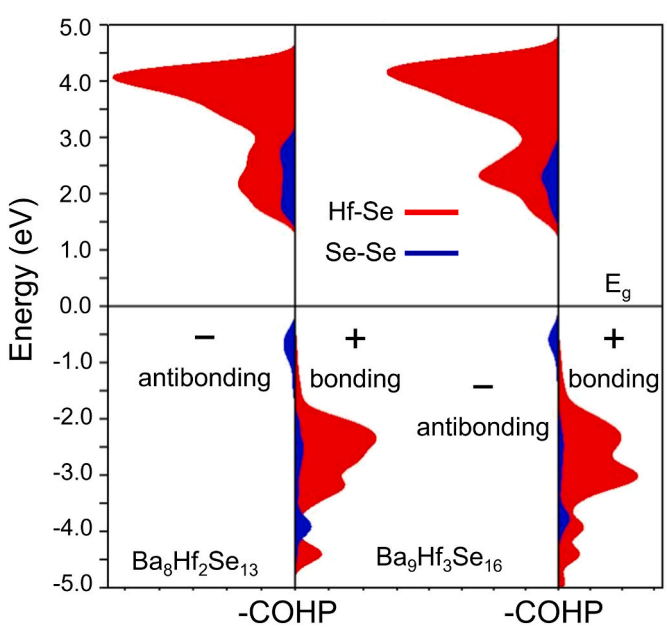

Fig. 6. Plots of Crystal Orbital Hamilton Populations (COHP) for the Hf–Se and Se–Se interactions in the (left) $Ba_8Hf_2Se_{11}(Se_2)$ and (right) $Ba_9Hf_3Se_{14}(Se_2)$ crystal structures.

4. Conclusions

Two new ternary selenides, $Ba_8Hf_2Se_{11}(Se_2)$ and $Ba_9Hf_3Se_{14}(Se_2)$, have been synthesized using high temperature reaction methods and represent the first reported compounds in the Ba-Hf-Se system. Their structures were probed by single crystal X-ray diffraction and structural refinements to consists of pseudo zero-dimensional structures with $(Se_2)^{2-}$ dimers. While $Ba_8Hf_2Se_{11}(Se_2)$ contains $[Hf_2Se_{11}]^{14-}$, the structure of $Ba_9Hf_3Se_{14}(Se_2)$ is built from a novel perovskite-type $[Hf_8Se_{36}]^{40-}$ cluster as well as isolated $[HfSe_6]^{8-}$ octahedra. The $[Hf_8Se_{36}]^{40-}$ cluster is notable in that it represents the perovskite-type analogue to the fully condensed version (i.e., $BaHfSe_3$) that is thermodynamically unstable and has yet to be synthesized. Interestingly, both compounds are calculated to exhibit small optical bandgaps (<2.0 eV) and strong optical absorption coefficients (>10^5 cm^{-1}), with relatively small electron effective masses in their conduction bands. Density functional theory calculations show the bandgap transitions stem from predominantly filled Se-4*p* to empty Hf-5*d* at the edges of their respective valence bands (VB) and conduction bands (CB). Thus, their underlying electronic structures and optoelectronic properties augurs well for the future potential of these and other non-perovskite type

chalcogenides in applications for solar energy conversion.

Supporting Information

The crystallographic data files of $Ba_8Hf_2Se_{11}(Se_2)$ and $Ba_9Hf_3Se_{14}(Se_2)$ structures are available by request to the Cambridge Crystallographic Data Centre (CCDC) in the form of crystallographic information files with CCDC numbers of 2272013 and 2274600, respectively. The data can be accessed from CCDC (https://www.ccdc.cam.ac.uk/) with no charge. The SEM data of the elemental composition, the Ba coordination environment, the atomic displacement parameters, and the metric details of $Ba_8Hf_2Se_{11}(Se_2)$ and $Ba_9Hf_3Se_{14}(Se_2)$ crystal structures are provided in the Supporting Information.

CRediT authorship contribution statement

Subhendu Jana: Investigation, synthesis, Formal analysis, Writing – review & editing. **Eric A. Gabilondo:** Data collection, Formal analysis. **Paul A. Maggard:** Conceptualization, computation, electronic structure, Formal analysis, Methodology, Writing – review & editing.

Declaration of competing interest

The authors declare that they have no known competing financial interests or personal relationships that could have appeared to influence the work reported in this paper.

Data availability

Data will be made available on request.

Acknowledgments

The authors acknowledge primary support of this work from the National Science Foundation (DMR-2317605). This work was performed in part by the Molecular Education, Technology and Research Innovation Center (METRIC) at NC State University, which is supported by the State of North Carolina. This work was also performed in part at the Analytical Instrumentation Facility (AIF) at North Carolina State University, which is supported by the State of North Carolina and the National Science Foundation (award number ECCS-2025064). The AIF is a member of the North Carolina Research Triangle Nanotechnology Network (RTNN), a site in the National Nanotechnology Coordinated Infrastructure (NNCI). The authors acknowledge the computing resources provided by the North Carolina State University High Performance Computing Services Core Facility.

Appendix A. Supplementary data

Supplementary data to this article can be found online at https://doi.org/10.1016/j.jssc.2023.124376.

References

[1] J. Rouxel, Low-dimensional solids: an interface between molecular and solid-state chemistry? The example of chainlike niobium and tantalum chalcogenides, Acc. Chem. Res. 25 (1992) 328–336.
[2] S. Jana, M. Ishtiyak, A. Mesbah, S. Lebègue, J. Prakash, C.D. Malliakas, J.A. Ibers, Synthesis and characterization of $Ba_2Ag_2Se_2(Se_2)$, Inorg. Chem. 58 (2019) 7837–7844.
[3] R. Sanjinés, H. Berger, F. Lévy, Synthesis and characterization of Nb_2Se_9 single crystals grown in molten solution, Mater. Res. Bull. 23 (1988) 549–553.
[4] A. Assoud, J. Xu, H. Kleinke, Structures and physical properties of new semiconducting polyselenides $Ba_2Cu_\delta Ag_{4-\delta}Se_5$ with unprecedented linear Se_3^{4-} units, Inorg. Chem. 46 (2007) 9906–9911.
[5] A. Assoud, S. Derakhshan, N. Soheilnia, H. Kleinke, Electronic structure and physical properties of the semiconducting polytelluride Ba_2SnTe_5 with a unique Te_5^{4-} unit, Chem. Mater. 16 (2004) 4193–4198.
[6] C.J. Warren, R.C. Haushalter, A.B. Bocarsly, Electrochemical synthesis of a pseudo-two-dimensional polytelluride containing Te_{12}^{2-} anions: structure of $[(C_2H_5)_4N]_2Te_{12}$, J. Alloys Compd. 233 (1996) 23–29.
[7] W.S. Sheldrick, M. Wachhold, Synthesis and structure of Cs_2Te_{13} and Cs_4Te_{28}, tellurium-rich tellurides on the methanolothermal route to Cs_3Te_{22}, Chem. Commun. (1996) 607–608.
[8] R. Patschke, P. Brazis, C.R. Kannewurf, M.G. Kanatzidis, $Cu_{0.66}EuTe_2$, KCu_2EuTe_4 and $Na_{0.2}Ag_{2.8}EuTe_4$: compounds with modulated square Te nets, J. Mater. Chem. 9 (1999) 2293–2296.
[9] M.C. Ohmer, R. Pandey, Emergence of chalcopyrites as nonlinear optical materials, MRS Bull. 23 (1998) 16–22.
[10] C. Zhou, Y.K. Lee, Y. Yu, S. Byun, Z.-Z. Luo, H. Lee, B. Ge, Y.-L. Lee, X. Chen, J. Y. Lee, O. Cojocaru-Mirédin, H. Chang, J. Im, S.-P. Cho, M. Wuttig, V.P. Dravid, M. G. Kanatzidis, I. Chung, Polycrystalline SnSe with a thermoelectric figure of merit greater than the single crystal, Nat. Mater. 20 (2021) 1378–1381.
[11] L.-D. Zhao, C. Chang, G. Tan, M.G. Kanatzidis, SnSe: a remarkable new thermoelectric material, Energy Environ. Sci. 9 (2016) 3044–3060.
[12] M. Zhou, K. Xiao, X. Jiang, H. Huang, Z. Lin, J. Yao, Y. Wu, Visible-light-responsive chalcogenide photocatalyst Ba_2ZnSe_3: crystal and electronic structure, thermal, optical, and photocatalytic activity, Inorg. Chem. 55 (2016) 12783–12790.
[13] M.A. Greaney, K.V. Ramanujachary, Z. Teweldemedhin, M. Greenblatt, Studies on the linear chain antiferromagnets: Ba_2MnX_3 (X = S, Se, Te) and their solid solutions, J. Solid State Chem. 107 (1993) 554–562.
[14] P.A. Maggard, J.D. Corbett, $Sc_5Ni_2Te_2$: synthesis, structure and bonding of a metal-metal-bonded chain phase, a relative of Gd_3MnI_3, Inorg. Chem. 38 (1999) 1945–1950.
[15] R. Xu, A. Husmann, T.F. Rosenbaum, M.-L. Saboungi, J.E. Enderby, P. B. Littlewood, Large magnetoresistance in non-magnetic silver chalcogenides, Nature 390 (1997) 57–60.
[16] P. Kumar, A. Kumar, S. Saha, D.V.S. Muthu, J. Prakash, S. Patnaik, U.V. Waghmare, A.K. Ganguli, A.K. Sood, Anomalous Raman scattering from phonons and electrons of superconducting $FeSe_{0.82}$, Solid State Commun. 150 (2010) 557–560.
[17] Y. Shinoda, Y. Okamoto, Y. Yamakawa, H. Matsumoto, D. Hirai, K. Takenaka, Superconductivity in ternary scandium telluride Sc_6MTe_2 with 3*d*, 4*d*, and 5*d* transition metals, J. Phys. Soc. Jpn. 92 (2023), 103701.
[18] N.A. Moroz, C. Bauer, L. Williams, A. Olvera, J. Casamento, A.A. Page, T.P. Bailey, A. Weiland, S.S. Stoyko, E. Kioupakis, C. Uher, J.A. Aitken, P.F.P. Poudeu, Insights on the synthesis, crystal and electronic structures, and optical and thermoelectric properties of $Sr_{1-x}Sb_xHfSe_3$ orthorhombic perovskite, Inorg. Chem. 57 (2018) 7402–7411.
[19] K. Hanzawa, S. Iimura, H. Hiramatsu, H. Hosono, Material design of green-light-emitting semiconductors: perovskite-type sulfide $SrHfS_3$, J. Am. Chem. Soc. 141 (2019) 5343–5349.
[20] D. Tiwari, O.S. Hutter, G. Longo, Chalcogenide perovskites for photovoltaics: current status and prospects, J Phys Energy 3 (2021), 034010.
[21] R. Lelieveld, D.J.W. IJdo, Sulphides with the $GdFeO_3$ structure, Acta Crystallogr. B 36 (1980) 2223–2226.
[22] T. Maekawa, K. Kurosaki, S. Yamanaka, Thermal and mechanical properties of perovskite-type barium hafnate, J. Alloys Compd. 407 (2006) 44–48.
[23] R. Vali, Structural phases of $SrHfO_3$, Solid State Commun. 148 (2008) 29–31.
[24] B.H. Chen, B.W. Eichhorn, P.E. Fanwick, Synthesis and structure of barium hafnium sulfides, $Ba_6Hf_5S_{16}$ and $Ba_5Hf_4S_{13}$: the n = 5 and 4 members of the $A_{n+1}B_nX_{3n+1}$ Ruddlesden-Popper phases, Inorg. Chem. 31 (1992) 1788–1791.
[25] B.-H. Chen, B. Eichhorn, Synthesis and structure of two new Ba_2MS_4 phases where M = Zr, Hf: a new series of K_2NiF_4 solids, Mater. Res. Bull. 26 (1991) 1035–1040.
[26] B.-H. Chen, W. Wong-Ng, B.W. Eichhorn, Preparation of new $Ba_4M_3S_{10}$ phases (M = Zr, Hf) and single crystal structure determination of $Ba_4Zr_3S_{10}$, J. Solid State Chem. 103 (1993) 75–80.
[27] K.V. Sopiha, C. Comparotto, J.A. Marquez, J.J.S. Scragg, Chalcogenide perovskites: tantalizing prospects, challenging materials, Adv. Opt. Mater. 10 (2022), 2101704.
[28] APEX3: Program for Data Collection on Area Detectors, Bruker AXS Inc., Madison, WI, USA..
[29] G.M. Sheldrick, XPREP Version 2008/2, Bruker AXS Inc., Madison, 2018.
[30] G.M. Sheldrick, Crystal structure refinement with *SHELXL*, Acta Crystallogr. C 71 (2015) 3–8.
[31] G.M. Sheldrick, A short history of *SHELX*, Acta Crystallogr. A 64 (2008) 112–122.
[32] A.L. Spek, Single-crystal structure validation with the program *PLATON*, J. Appl. Crystallogr. 36 (2003) 7–13.
[33] L.M. Gelato, E. Parthé, *STRUCTURE TIDY* – a computer program to standardize crystal structure data, J. Appl. Crystallogr. 20 (1987) 139–143.
[34] G. Kortüm, Reflectance Spectroscopy: Principles, Methods, Applications, Springer-Verlag, New York, 1969.
[35] P. Makuła, M. Pacia, W. Macyk, How to correctly determine the band gap energy of modified semiconductor photocatalysts based on UV–vis spectra, J. Phys. Chem. Lett. 9 (2018) 6814–6817.
[36] G. Kresse, J. Furthmüller, Efficient iterative schemes for *Ab Initio* total-energy calculations using a plane-wave basis set, Phys. Rev. B Condens. Matter 54 (1996) 11169–11186.
[37] G. Kresse, J. Furthmüller, Efficiency of *Ab-initio* total energy calculations for metals and semiconductors using a plane-wave basis set, Comput. Mater. Sci. 6 (1996) 15–50.
[38] J.P. Perdew, K. Burke, M. Ernzerhof, Generalized gradient approximation made simple, Phys. Rev. Lett. 77 (1996) 3865–3868.
[39] Y. Hinuma, G. Pizzi, Y. Kumagai, F. Oba, I. Tanaka, Band structure diagrams paths based on crystallography, Comput. Mater. Sci. 128 (2017) 140–184.

[40] R. Dronskowski, P.E. Bloechl, Crystal orbital Hamilton populations (COHP). Energy-resolved visualization of chemical bonding in solids based on density-functional theory calculations, J. Phys. Chem. 97 (1993) 8617–8624.
[41] V.L. Deringer, A.L. Tchougréeff, R. Dronskowski, Crystal orbital Hamilton population (COHP) analysis as projected from plane-wave basis sets, J. Phys. Chem. A 115 (2011) 5461–5466.
[42] S. Maintz, V.L. Deringer, A.L. Tchougréeff, R. Dronskowski, Analytic projection from plane-wave and PAW wavefunctions and application to chemical-bonding analysis in solids, J. Comput. Chem. 34 (2013) 2557–2567.
[43] S. Maintz, V.L. Deringer, A.L. Tchougréeff, R. Dronskowski, LOBSTER: a tool to extract chemical bonding from plane-wave based DFT, J. Comput. Chem. 37 (2016) 1030–1035.
[44] R. Nelson, C. Ertural, J. George, V.L. Deringer, G. Hautier, R. Dronskowski, LOBSTER: local orbital projections, atomic charges, and chemical-bonding analysis from projector-augmented-wave-based density-functional theory, J. Comput. Chem. 41 (2020) 1931–1940.
[45] K.O. Klepp, D. Sturmayr, Crystal structure of sodium copper triselenohafnate(IV), $NaCuHfSe_3$, Z, Für Krist. - New Cryst. 212 (1997) 75.
[46] A. Kolb, K.O. Klepp, Quaternary chalcogenides of the IVa metals with layered structures: preparation and crystal structure of $NaCuHf_2Se_5$, Solid State Sci. 5 (2003) 1027–1031.
[47] L. Pauling, Atomic radii and interatomic distances in metals, J. Am. Chem. Soc. 69 (1947) 542–553.
[48] J. Prakash, A. Mesbah, J. Beard, S. Lebègue, C.D. Malliakas, J.A. Ibers, Synthesis, crystal structure, optical, and electronic study of the new ternary thorium selenide $Ba_3ThSe_3(Se_2)_2$, J. Solid State Chem. 231 (2015) 163–168.
[49] Y. Park, M.G. Kanatzidis, On the dissolution of gold in K_2Q_x and Na_2Q_x fluxes (Q=S, Se). Formation of $KAuS_5$, $KAuSe_5$, $CsAuSe_3$, $KAuSe_2$ and $NaAuSe_2$: low-dimensional Au^+ and Au^{3+} compounds with poly- and mono-chalcogenide ligands, J. Alloys Compd. 257 (1997) 137–145.
[50] P. Böttcher, J. Getzschmann, R. Keller, Zur Kenntnis der Dialkalimetalldichalkogenide β-Na_2S_2, K_2S_2, α-Rb_2S_2, β-Rb_2S_2, K_2Se_2, Rb_2Se_2, α-K_2Te_2, β-K_2Te_2 und Rb_2Te_2, Z. Anorg. Allg. Chem. 619 (1993) 476–488.
[51] K.-S. Choi, M.G. Kanatzidis, Si extraction from silica in a basic polychalcogenide flux. Stabilization of $Ba_4SiSb_2Se_{11}$, a novel mixed selenosilicate/selenoantimonate with a polar structure, Inorg. Chem. 40 (2001) 101–104.
[52] R. Yue, A.T. Barton, H. Zhu, A. Azcatl, L.F. Pena, J. Wang, X. Peng, N. Lu, L. Cheng, R. Addou, S. McDonnell, L. Colombo, J.W.P. Hsu, J. Kim, M.J. Kim, R.M. Wallace, C.L. Hinkle, $HfSe_2$ thin films: 2D transition metal dichalcogenides grown by molecular beam epitaxy, ACS Nano 9 (2015) 474–480.
[53] A. Abudurusuli, H. Ding, K. Wu, Synthesis and characterization of two lead-containing metal chalcogenides: $Ba_5Pb_2Sn_3S_{13}$ and $Ba_6PbSn_3Se_{13}$, J. Solid State Chem. 255 (2017) 133–138.
[54] J.P. Perdew, Density functional theory and the band gap problem, Int. J. Quant. Chem. 28 (1985) 497–523.
[55] A. Swarnkar, W.J. Mir, R. Chakraboty, M. Jagadeeswararao, T. Sheikh, A. Nag, Are chalcogenide perovskites an emerging class of semiconductors for optoelectronic properties and solar cell? Chem. Mater. 31 (2019) 565–575.
[56] P.C. Müller, C. Ertural, J. Hempelmann, R.D. Dronskowski, Crystal orbital bond index: covalent bond orders in solids, J. Phys. Chem. C 125 (2021) 7959–7970.